



Piezo-phototronic effect enhanced performance of a p-ZnO NW based UV–Vis–NIR photodetector

Zhihao Huo^{a,b,1}, Yufei Zhang^{a,b,1}, Xun Han^{a,1}, Wenqiang Wu^a, Wenkai Yang^{a,b},
Xiandi Wang^{a,*}, Mengmeng Zhou^{c,*}, Caofeng Pan^{a,b,**}

^a CAS Center for Excellence in Nanoscience, Beijing Key Laboratory of Micro-nano Energy and Sensor, Beijing Institute of Nanoenergy and Nanosystems, Chinese Academy of Sciences, Beijing 100083, PR China

^b School of Nanoscience and Technology, University of Chinese Academy of Sciences, Beijing 100049, PR China

^c ARC Research Hub for Computational Particle Technology, Department of Chemical Engineering, Monash University, Clayton, Victoria 3800, Australia

ARTICLE INFO

Keywords:

Photodetector
P-ZnO/Al₂O₃/n-Si
A broad spectral range
UV–Vis–NIR
Tunneling effect
Piezo-phototronic effect

ABSTRACT

ZnO, as a potential candidate, has attracted extensive attention in optoelectronics, energy systems and other fields. However, the wide bandgap of ZnO severely limits its application in a wide range of photoresponse, and preparing p-type ZnO is another stumbling block that hinders the development of ZnO-based devices. Here, a high-performance photodetector with a wider spectral detection range from UV–vis to NIR builds on the structure of p-ZnO/Al₂O₃/n-Si is fabricated. The PD exhibits a marked sensitivity (75,000%), excellent responsivity (13.80 A W⁻¹, 365 nm), high specific detectivity (> 10¹² Jones), fast response (< 100 μs), which indicates that inserting an insulated Al₂O₃ layer between an n-type semiconductor and a p-type semiconductor is a fruitful method to enhance carriers separation and collection efficiency. The carrier transport mechanism at the interface of PDs with different Al₂O₃ thickness is based on the quantum mechanical of Fowler-Nordheim tunneling or direct tunneling. Additionally, the overall signal levels of the photodetector could be further optimized using the piezo-phototronic effect. This study demonstrates an alternative route to implement high-efficiency photodetectors with a broader response range and provides an in-depth understanding of regulating carrier tunneling of the p-ZnO/Al₂O₃/n-Si heterojunction using the piezo-phototronic effect.

1. Introduction

Photodetectors (PDs) with a broad range of sensing capabilities from ultraviolet (UV) to near-infrared (NIR) are extremely critical in various industrial and scientific applications, including visual imaging, environmental monitoring, optical communication, and military tracking [1–5]. Commercial photodetectors currently used to detect sub-bands regions in the UV to the NIR range rely mainly on single photosensitive semiconductor material, for example, GaN (< 400 nm), Si (400–1100 nm) and InGaAs (800–1600 nm) [6–8]. Considerable efforts have been implemented to extend the operating wavelength range and optimize the capability of PDs. Several novels and high-profile materials such as perovskite [9–11], pyroelectric material [12], organic materials [13,14], and 2D materials [15,16] demonstrate a certain potential in

broad spectral detection, however, they struggle to achieve outstanding overall performance for their respective defects, ambient instability, or complex preparation processes.

ZnO with wurtzite structure has been widely studied in optoelectronic devices [17–19], energy devices [20–23], transistor [24,25] and sensors [26–30], especially in room-temperature UV detection due to the wide bandgap (3.37 eV) and the high exciton-binding energy (60 meV) [31–33]. Some excellent studies have shown that a structure integrated with ZnO compensates for the limited light absorption properties of a single material, which provides a novel platform/method to achieve a wider detection range [4,34,35]. However, the reliable manufacture of p-type ZnO is still an enormous challenge for ZnO-based optoelectronic devices in practical applications [36,37]. Recently, our group indicated that the antimony (Sb) is a highly promising candidate

* Corresponding authors.

** Corresponding author at: CAS Center for Excellence in Nanoscience, Beijing Key Laboratory of Micro-nano Energy and Sensor, Beijing Institute of Nanoenergy and Nanosystems, Chinese Academy of Sciences, Beijing 100083, PR China.

E-mail addresses: xiandiwang@zju.edu.cn (X. Wang), mengmeng.zhou@monash.edu.com (M. Zhou), cspan@binn.cas.cn (C. Pan).

¹ Zhihao Huo, Yufei Zhang and Xun Han contributed equally to this work.

for producing reliable p-ZnO nanowires (NWs), and Sb-ZnO NWs have outstanding piezoelectric properties for non-central symmetric structure [38]. This adds a significant and trustworthy scientific basis for studying the piezo-phototronic effect of p-ZnO NWs [39–42]. Meanwhile, silicon (Si) as a primary material in the electronic industry for sensing the visible (vis) light is breaking through the constraints of indirect absorption mechanism, lack of tunability and highly reflective surface, seeking a place in broadband detection [35,43,44].

In this work, we demonstrate an ultrahigh-sensitivity PD with extraordinary optoelectronic performances for UV–vis–NIR light on account of the p-ZnO/Al₂O₃/n-Si heterostructure. The intervention of the insulating Al₂O₃ layer makes the separation and collection of photoexcited carriers more efficient at reverse bias [45]. Experimental results indicate that the PD with 8 nm Al₂O₃ has a fast response time, high responsivity, excellent detectivity over the broad spectral range from the UV to the NIR. And the maximum sensitivity reached 75,000% under 365 nm light with a power density of 26.52 mW cm⁻². To our knowledge, this is currently the highest value among PDs about ZnO NW arrays. The carrier tunneling mechanisms of devices with different thicknesses of the Al₂O₃ layer are investigated to better interpret the extraordinary optoelectronic performance. Moreover, the piezo-phototronic effect of coupling semiconductor properties, photon excitation and piezoelectric polarization was further utilized to tune the carriers transport and tunneling barrier distance at the interface/junction [39,46].

2. Experimental section

2.1. Construction process of the device

First, the n-type double-side polished single-crystalline silicon wafer (orientation (100), 1–20 Ω cm, 300 μm thickness) was etched for 30 min with 5 vol% isopropanol and 3 wt% KOH. These substrates were then ultrasonically cleaned in acetone, isopropanol, and distilled water for 5 min. Subsequently, the substrates were coated with Al₂O₃ by atomic layer deposition (SUNALETMR-200). Then, a ZnO seed layer was sputtered on the sample by radio frequency (RF) magnetron sputtering (PVD75 Kurt J. Lesker). Next, putting the coated n-Si wafer into the mixed doping solution composed of 25 mM Zn(NO₃)₂, 25 mM hexamethylenetetramine, and Sb-dopant solution in a mechanical convection oven at 95 °C for 24 h. The Sb-dopant solution contains sodium glycolate and antimony acetate in a ratio of 12:1, and sodium glycolate is synthesized from equimolar sodium hydroxide and glycolic acid. An AZO thin layer as top electrodes was deposited on p-ZnO and a layer of Al on the n-Si wafer as bottom electrodes. Finally, a thin layer of polydimethylsiloxane (PDMS) is spin-coated to encapsulate the device.

2.2. Characterization and measurements of materials

X-ray Diffraction (X'Pert 3 Powder) θ - 2θ scanning with Cu-K α radiation source was used to characterize the crystallization of the film. Detailed microstructures were characterized by Field-Emission Scanning Electron Microscopy (FESEM) (Hitachi SU8020), HRTEM (FEI F30) with energy-dispersive X-ray spectroscopy (EDX), and transmission electron microscopy (TEM) (Tecnai G2). External strain is applied to the device through a 3D mechanical stage (movement resolution close to 10 μm). The electric characteristics of the PD were measured via a Keithley 4200 parameter analyzer, a synthesized function generator (Model No. DS345, Stanford Research Systems, Inc.), and a low-noise current pre-amplifier (Model No. SR570, Stanford Research Systems, Inc.). The absorption and transmission spectra of the devices were obtained by a UV–vis–NIR spectrophotometer (Shimadzu UV 3600). An MLL-III-633–300 mW 633 nm and MLL-III-1064–300 mW 1064 nm light (Changchun New Industries Optoelectronics Technology Co., Ltd.) served as the irradiation source. Also, the periodic switching characteristics of the PDs at different operating frequencies were measured

with an optical chopper (SR540, Stanford Research Systems, Inc.).

3. Results and discussion

The structure and manufacturing process of the typical p-ZnO/Al₂O₃/n-Si UV–vis–NIR photodetector are shown in Fig. 1a. A polished n-Si wafer was first cleaned ultrasonically by acetone, isopropyl alcohol and deionized water. Secondly, the surface of the wafer was etched into many small tetrahedrons by wet chemical etching to obtain the effective surface area for improving the light absorption efficiency (Fig. 1b). Thirdly, an alumina (Al₂O₃) layer was deposited on the wafer via the atomic layer deposition technique. Fourthly, an ultrathin ZnO seed layer was sputtered for low-temperature hydrothermal synthesis of Sb-doped p-ZnO NW arrays. Fifthly, the top electrode (AZO) on the p-ZnO NW arrays and Al electrode on the n-Si substrate was deposited separately by RF magnetron sputtering (Fig. S1, Supporting Information). A thin polydimethylsiloxane (PDMS) layer was finally rotated to encapsulate the PD. The experimental section provides a more detailed discussion. Fig. 1c shows the scanning electron microscopy (SEM) images of Sb-doped p-ZnO NWs, indicating highly clustered ZnO NWs grown along the c-axis and perpendicular to the n-Si surface with a micro-pyramid, with a length of 3 μm and a diameter of about 150 nm. Fig. 1d illustrates the SEM diagram after the deposition of AZO on the top of ZnO. The uneven surface of the device greatly increases light absorption. Fig. 1e shows the X-ray diffraction (XRD) pattern of the p-ZnO NWs array. Obviously, the sample has a strong peak at 34.5°, which corresponds to the piezoelectric property of the ZnO (0002) plane. To clarify the composition uniformity of the heterojunction, the energy dispersive X-ray spectrum (EDX) of p-ZnO NWs is obtained, as demonstrated in Fig. 1f. It exhibits that the Sb content in ZnO was identified to be about 1.25% despite the concentration of doping solution was only 1% (Table S1). Fig. 1g illustrates a cross-sectional transmission electron microscopy (TEM) image of the interface between the heterojunction, where the thin Al₂O₃ layer has a thickness of approximately 8 nm. Besides, an EDX line scan profile across the heterojunction along the red line demonstrates elementary distribution and the thickness of the Al₂O₃ layer could also obtain from the scan data (Fig. 1h).

A photodetector with ultrahigh sensitivity and fast response of sensing wide spectrum response from UV–vis to NIR was constructed. As shown in Fig. 2a, the absorption of devices with Si micro-pyramids in longer wavelength regions significantly increases, and further increase present in the p-ZnO/Al₂O₃/n-Si junction. Besides, the p-ZnO NWs array absorbs most of 365 nm wavelength light, has 39% transmittance for 633 nm wavelength light and is the transparent wavelength and little absorption in the 1064 nm, as depicted in Fig. S2. (365 nm light as UV source, 633 nm light as vis source, and 1064 nm light as NIR source). This indicates that photo-generated carriers mainly come from the p-ZnO side under UV irradiation, come from the n-Si side under NIR irradiation, and come from both sides under vis irradiation. Fig. 2b illustrates the *I*-*V* characteristic of the heterojunction at dark and the irradiation of UV–vis–NIR with 2 mW cm⁻². We can observe that the device presents a typical rectifying characteristic and has more intensely photosensitive properties at reverse bias. Also, a series of *I*-*V* characteristics under the UV–vis to NIR irradiation with different power density is plotted in Fig. S3. The photocurrent ($I = I_{\text{light}} - I_{\text{dark}}$ [35], I_{light} and I_{dark} are output currents with and without light irradiation, respectively) increases with the optical power density under irradiation of UV–vis or NIR range. Significantly, the absolute current increases from 1.42 μA (dark current) to 1.06 mA under 26.52 mW cm⁻² of 365 nm light, to 0.32 mA under 8.79 mW cm⁻² of 633 nm light, and to 0.44 mA under 14.5 mW cm⁻² of 1064 nm light. The sensitivity defined as $(I_{\text{light}} - I_{\text{dark}})/I_{\text{dark}}$ of devices under the irradiation of various power densities of UV–vis–NIR at -2 V bias is integrated and plotted in Fig. 2c. Under the irradiation of each light, the sensitivity of devices increases as the increasing incident optical power density. And the sensitivity of the PD with 8 nm Al₂O₃ reached 50,000% under UV irradiation with

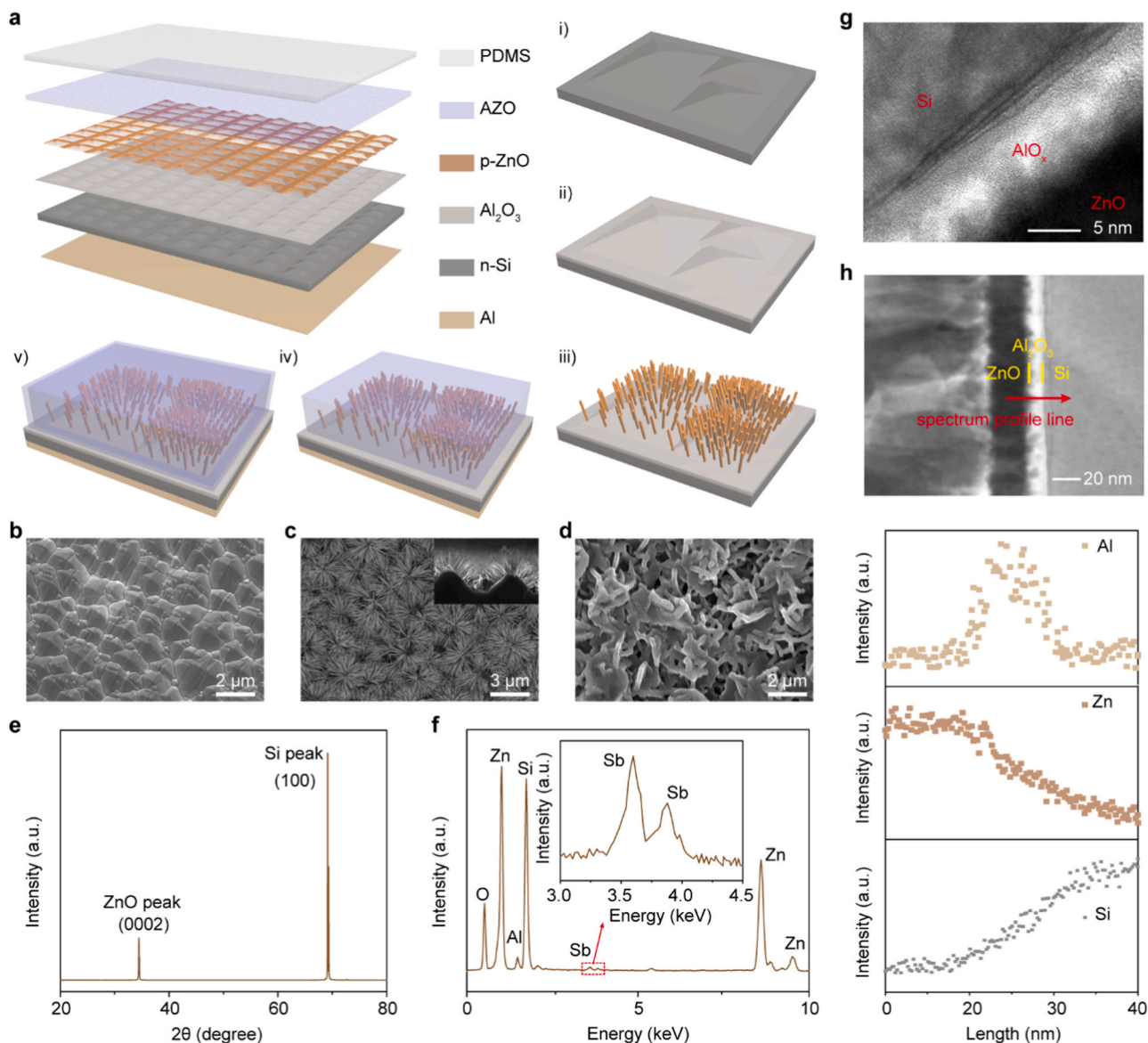


Fig. 1. Device structure and characterizations. (a) Schematic illustration and fabrication process of the p-ZnO/Al₂O₃/n-Si heterojunction. (b) SEM images of n-Si micropyramid. (c) Top view SEM images of p-ZnO NWs array. Inset: Side view SEM image of p-ZnO NWs. (d) AZO coating as the top electrode. (e) XRD pattern of the p-ZnO NWs and n-Si. (f) Energy-dispersive X-ray spectroscopy of the PD. (g) TEM images of the cross-section of a heterojunction with 8 nm Al₂O₃ thickness. (h) The spectral profile of the cross-section of the heterojunction. The red line in the figure is the path of data acquisition. (For interpretation of the references to color in this figure legend, the reader is referred to the web version of this article.)

12.53 mW cm⁻² and further to 75,000% at 26.52 mW cm⁻² (Fig. S4), which is the highest compared to other nanostructure PDs [47–50]. Besides, the sensitivity of the device is 22,000% under 633 nm irradiation and 31,000% under 1064 nm irradiation. These parameters are 34.5, 5.4, and 47.5 times larger than the PD without Al₂O₃ under the corresponding light excitation (Fig. 2c). The photoresponse of the device at a frequency range of 5–800 Hz under the irradiation with 2 mW cm⁻² of wide range light is measured and manifested in Fig. 2d. The response time significantly decreases as the on-off frequency increases regardless of the illumination wavelength in the UV–vis to the NIR range. The rise time refers to the time for the response to rise from 10% to 90% of the peak, and the fall time refers to the time for the response to fall from 90% to 10% of the peak [31]. Remarkably, the output of the PD realizes the switch of steady-state photocurrent and dark current even if the switching frequency of the optical signal is at 800 Hz (Fig. S5). Fig. 2e shows the current output curves of the PD under different light. The rise time respectively is 180 μs for UV light, 130 μs for vis light and 140 μs

for NIR light, and the fall time is 230 μs, 70 μs and 180 μs for UV light, vis light and NIR light, respectively. In a word, the p-ZnO/Al₂O₃/n-Si PD exhibits a dramatically rapid response behavior under the irradiation of UV–vis to the NIR lights.

To thoroughly understand the carrier transport mechanisms and optoelectronic performances of the PD, we systematically investigate the p-ZnO/Al₂O₃/n-Si with various insulating barrier thicknesses from 0 nm to 10 nm. As we all know, the quantum tunneling effect refers to the behavior of particles penetrating or crossing potential barriers to exceed their kinetic energy. Fig. 3a illustrates three typical transport mechanisms, direct tunneling (DT) under low voltage, Fowler-Nordheim tunneling (FNT) under a high bias voltage regime and temperature-dependent thermionic emission [51,52]. To explain the transport mechanism more intuitively, it is necessary to understand the energy levels of each material (Fig. 3b). The conduction band and valence band of the ZnO, Al₂O₃ and Si are –4.35 eV and –7.72 eV, –1.35 eV and –8.15 eV, –5.17 eV and –4.05 eV, versus vacuum, respectively [53].

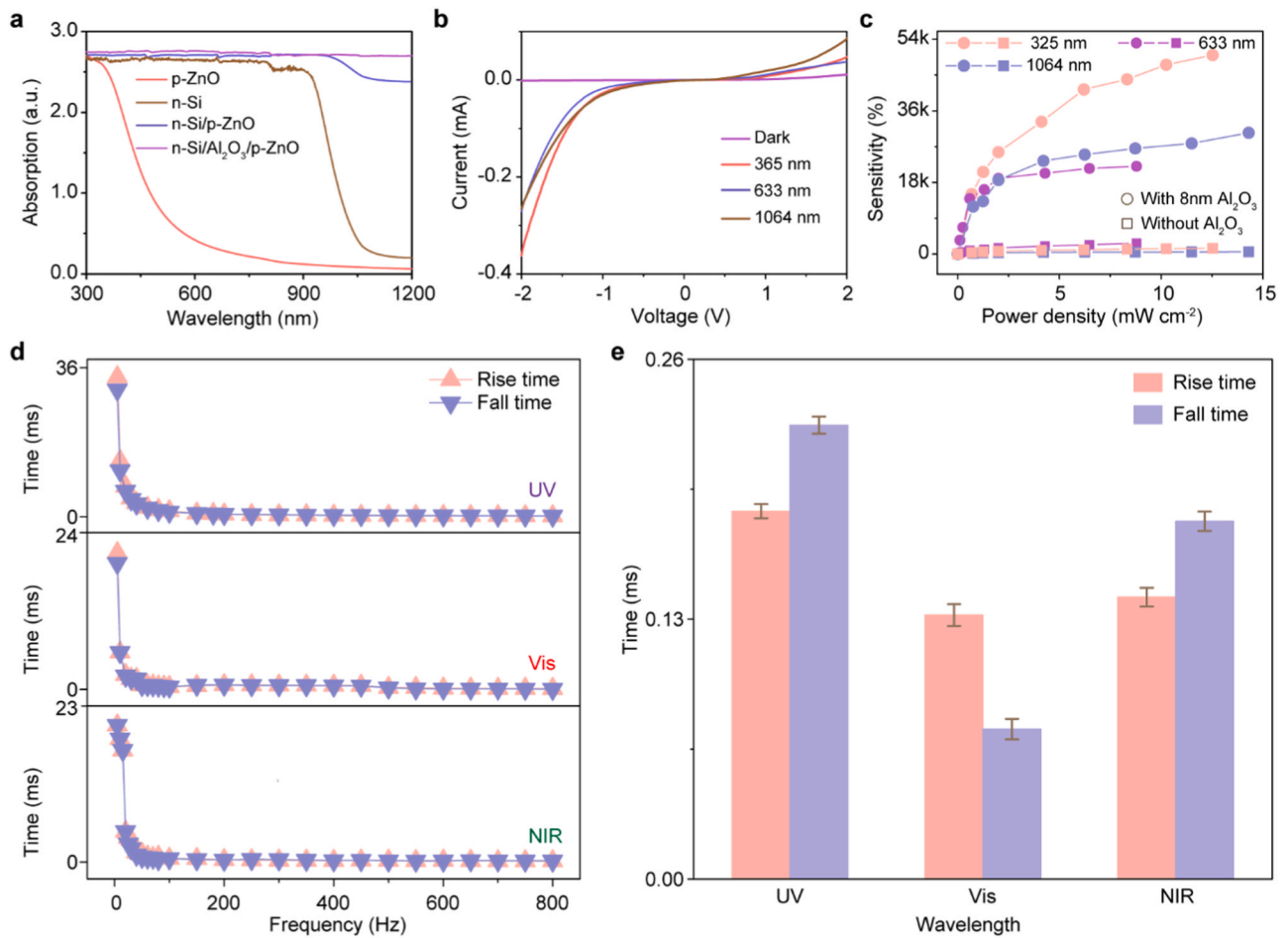


Fig. 2. Optical properties and response speed of PDs. (a) Absorption spectra of p-ZnO, n-Si, p-ZnO/n-Si and the p-ZnO/Al₂O₃/n-Si devices. (b) *I-V* characteristics of the p-ZnO/Al₂O₃/n-Si PD under dark and the illumination of UV–vis–NIR with the power densities of 2 mW cm⁻², respectively. (c) The sensitivity of PDs with various structures under the excitation of 365 nm light. (d) Plot of the response time as a function of on/off frequency under the three given wavelengths. (e) Response time of the PD under UV light, Vis light and NIR light with 2 mW cm⁻² at -2 V (97.5% confidence interval).

Under thermal equilibrium, the Si and ZnO sides will form a depletion zone due to the diffusion of carriers, which makes the Fermi energy level in the whole heterojunction region stabilized. Fig. 3c demonstrates the energy band of the heterojunction under forward bias. Electrons in Si and holes in ZnO will be collected through DT or FNT events under the dominance of the external electric field. Specifically, when the applied voltage is less than the barrier height ϕ_1 , the electric field-induced barrier will not be severely deformed and direct tunneling dominates the transport of carriers. The DT current (I_{DT}) linearly depends on the bias, given by [51,54].

$$I_{DT} \propto V \exp \left[\frac{-4\pi d \sqrt{m_0 \phi_B}}{h} \right] \quad (1)$$

where m_0 , ϕ_B , h , d are the effective electron mass, tunneling barrier, the Plank constant and the tunneling thickness, respectively. When the external voltage exceeds ϕ_1 , which is enough to modify the barrier bend into a triangle, and FNT becomes the dominant mechanism. The tunneling current (I_{FNT}) and applied bias (V) comply with the following principles [51,54].

$$I_{FNT} \propto V^2 \exp \left[-\frac{8\pi d \sqrt{2m_0 \phi_B^3}}{3heV} \right] \quad (2)$$

According to the above formula (2) and the *I-V* characteristics of devices (Fig. S6), the plot of $\ln(I/V^2)$ versus V^{-1} for alumina of different thickness is calculated and integrated, as demonstrated in Fig. 3d. In

comparison, the device with 2 nm thick alumina behaved like a conventional semiconductor diode with rectifying characteristics but other devices did not. Also, we notice that the plot of $\ln(I/V^2)$ versus V^{-1} is a strong linear relationship with a negative slope for FNT at a high voltage and the slope of DT increases exponentially at a low bias for devices with 4 nm, 6 nm, or 8 nm thick alumina. Besides, the qualification of the FNT mechanism is lost for the device with 10 nm Al₂O₃ (Fig. S7). More specifically, FNT is particularly effective for 4 nm and 6 nm devices, but its activation is weak for an 8 nm device and completely ineffective for devices with thicker films. Fig. 3e shows the transition voltage (V_{trans}) of several devices from DT to FNT, defined as $V_{trans} = \phi_B/e$ [52]. The V_{trans} increases from 0.29 V to 0.88 V as the thickness of alumina increases, which indicates that the triggering FNT requires greater bias as the thickness increases. Actually, thermionic emission strongly dependent on temperature is another important mechanism for carriers to pass through the potential barrier. The relatively weak temperature-dependence electrical properties further prove that the device with 8 nm Al₂O₃ is governed by FNT in a strong electric field and DT at a lower voltage (Fig. S8). Then, the photoresponse of devices with various thickness under UV fixed irradiation of 2 mW cm⁻² was studied and contrasted (Fig. S6). The samples using the Al₂O₃ layer as the current blocking layer reveals more excellent photoelectric behavior, especially under the reverse bias. After the introduction of Al₂O₃, the accumulation of space charges is inhibited and the trap state on the surface is reduced. On the other hand, Al₂O₃ may reduce interface-related defects and optimize the p-ZnO/n-Si interface, which

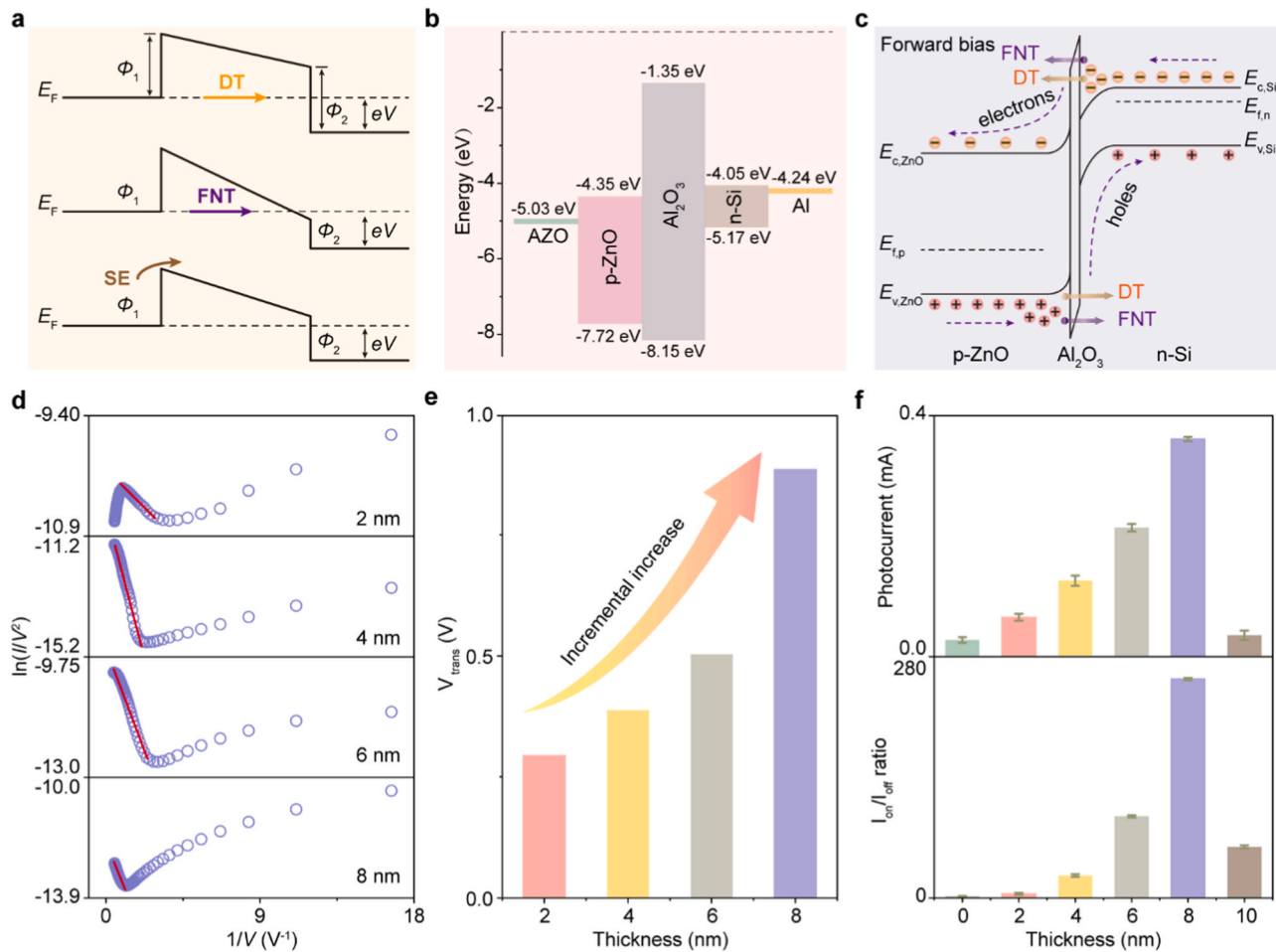


Fig. 3. Thickness-dependent charge transport mechanisms of the junction. (a) Schematic diagram of three tunneling mechanisms. (b) Energy band diagram of the PD with 8 nm Al_2O_3 under thermal equilibrium. (c) Schematic diagram of carrier transport of device under forward bias. (d) $\ln(I/V^2)$ vs. $1/V$ plots, reconfigured from I - V characteristics of different Al_2O_3 thicknesses at room temperature. The distinct linear response indicates that FNT is the leading quantum transport mechanism through the junctions. The linear fitting curves with FNT current (red line). (e) The transition voltage from DT to FNT as a function of the thickness of Al_2O_3 . (f) The photocurrent and on/off current ratio of different devices varies with the thickness of Al_2O_3 (97.5% confidence interval). (For interpretation of the references to color in this figure legend, the reader is referred to the web version of this article.)

may also be the reason for the sensitivity to vis light. When the Al_2O_3 thickness is small, photocarriers and dark-state carriers could tunnel through the Al_2O_3 layer through FNT or DT. If the Al_2O_3 layer is too thick, dark-state carriers could tunnel through the Al_2O_3 layer via DT, and the tunneling probability of photo-excited and the dark-state carriers is reduced. Therefore, a suitable thickness is essential for achieving a remarkable optoelectronic property of devices. Fig. 3f illustrates the photocurrent and on/off current ratio of these devices as a function of the thickness of the insulating layer, both first increase and then decrease with the thickness increase. The optoelectronic property of the device is the best when the thickness of alumina is 8 nm, with a switch ratio of 256, a photocurrent of 0.36 mA, and a dark current of only 1.42 μA .

Piezo-phototronic effect, a coupling effect of piezoelectricity, semiconductor, and photoexcitation, was further utilized to modulate the transport of electron-hole pairs to enhance/optimize the PD performance [39]. We define the compressive strain as negative [38]. Fig. S9 illustrates the application details of the compression strains [46]. Fig. 4a-c presents the strain-dependent carrier transport properties under the irradiation with 2 mW cm^{-2} . As strains go higher from 0‰ to -0.79‰, the output current gradually increases regardless of UV-vis or NIR light. Fig. 4d-f shows the photocurrent under various compressive strains as a function of the incident optical power density. Obviously, the photocurrent rises as the power density increases and presents a trend of

slow growth at higher power density when the samples are illuminated at UV light. When the sample is illuminated at vis light, the photocurrent reaches a saturation limit at low power (2 mW cm^{-2}) and there is no further increase as the power density increases (Fig. 4d). And unlike that, the current suddenly increases under NIR light with high power levels (Fig. 4f). Under -2 V bias and the irradiation wavelength in the UV-vis to the NIR range, the photocurrent under different compressed strains from 0‰ to -0.79‰ is plotted in Fig. 4g-i. The photocurrent is gradually improved as compressive strains increases, and it exhibits a better linear relationship evenly for the UV-vis to NIR range. At the same time, the overall signal level is significantly increased because more photocarriers are generated under the light with a higher power density. In other words, the photoresponse of the PD is enhanced utilizing the piezo-phototronic effect.

As the critical figure-of-merits to evaluate the capability of PDs, the responsivity (R) and specific detectivity (D^*) are analyzed, they can be expressed as follows [32].

$$R = \frac{I_{\text{light},s} - I_{\text{dark},s}}{P_{\text{ill}}} = \frac{\eta_{\text{ext}} q \Gamma_G}{h\nu} \quad (3)$$

$$D^* = \frac{R}{(2qI_{\text{dark},s}/S)^{1/2}} \quad (4)$$

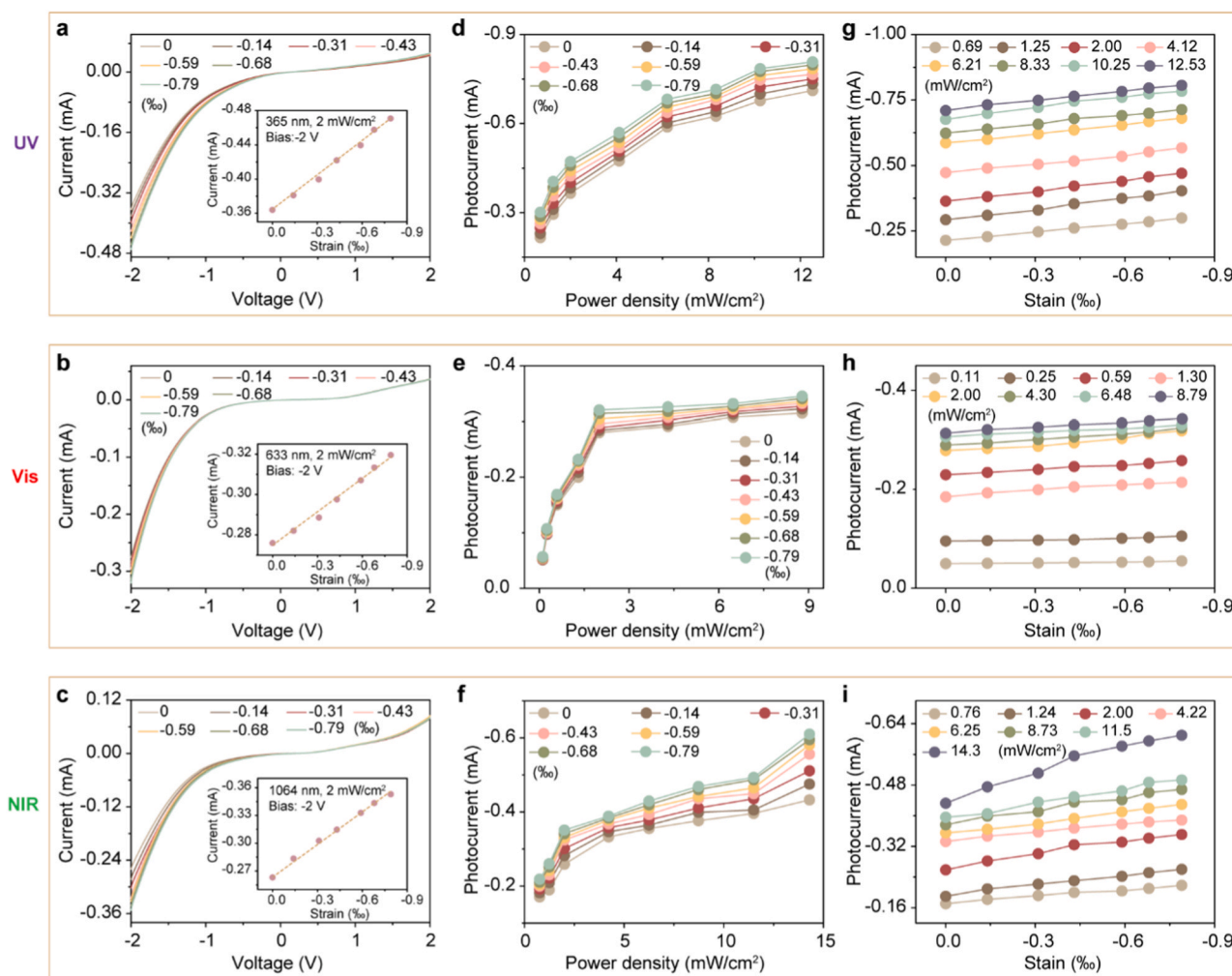


Fig. 4. The modulation of photoresponse by the piezo-phototronic effect. Typical I - V characteristics of the PD under different compressive strains, excited by (a) 365 nm light, (b) 633 nm light and (c) 1064 nm light with 2 mW cm^{-2} , respectively. Inset shows the current change with strain under corresponding conditions. The plot of photocurrent under different strain as a function of illumination conditions at (d) 365 nm light, (e) 633 nm light and (f) 1064 nm light. Photocurrent under illumination conditions as a function of strains at (g) 365 nm light, (h) 633 nm light and (i) 1064 nm light.

where $P_{\text{in}} = I_{\text{in}} \times S$ is the incident power on the PD, q , η_{ext} , h , ν , Γ_G , I_{in} and S are the electronic charge (1.6×10^{-19} Coulombs), the external quantum efficiency (EQE), Planck's constant, the frequency of the light, the internal gain, the illumination power density and the effective area of the photodetector in cm^2 , respectively. The R and D^* under the UV-vis to NIR range with various optical power density and compressive strains at -2 V are plotted in Fig. 5a-c, respectively. The R increases with compressive strains increase from 0‰ to -0.79% or the incident optical power density decreases, and no saturation occurs whether under the illumination in UV-vis or NIR light. Besides, the device has a responsivity of 9.90 A W^{-1} and EQE of 3360% at high UV irradiation power (12.53 mW cm^{-2}) without strain (Fig. 5a), which is much better than other or commercial UV PDs [16,32]. And maximum responsivity is 13.80 A W^{-1} under the 0.69 mW cm^{-2} and a -0.79% compressive strain. In the same case, the extreme value of D^* is as high as 3.12×10^{12} Jones. Besides, similar variation trends of R as various strains and power density could be observed under the irradiation of vis and NIR light. Under vis irradiation, the R and D^* reach the extreme values of 10.60 A W^{-1} and 3.55×10^{12} Jones under -0.79% strain with 0.08 mW cm^{-2} , respectively (Fig. 5b). The extreme value of R and D^* are above 16.30 A W^{-1} and 2.70×10^{12} Jones under NIR irradiation, respectively (Fig. 5c). Noticeably, these excellent parameters are much larger than the p-ZnO/n-Si PD (Fig. S10), and even higher than most reported ZnO-based PDs or other types of PDs (Table 1), which

demonstrates that our PD has a significant and remarkable detection capability spanning the full range from UV-vis to NIR. To specifically interpret the piezo-phototronic effect on the responsivity, the relative change is defined as $\Delta R/R_0 \times 100\%$ ($\Delta R = R_S - R_0$, R_0 is the responsivity without strain and R_S is the responsivity at a compressive strain) under compressive strain are shown in Fig. S11. The maximum enhancement of R by UV-vis and NIR irradiation under relatively small strain reached 39.7%, 21.8% and 41.0%, respectively. Similarly, the relative change of specific detectivity as compressive strain at various optical power density is also shown in Fig. S11, which demonstrates the regulation of the piezoelectric potential on specific detectivity under external strains. In addition, in order to further understand the effect of strains on devices, we have summarized some key parameters of devices, as shown in Table S2.

To further elucidate the underlying physical processes of the carrier transport in detail, the energy band diagram of the PD under various strains and light excitation is plotted in Fig. 6. When the energy of the incident photon is greater than the forbidden bandwidth of the material, the electrons in the active region such as the p-side/n-side are excited to produce a mass of photo-excited electron-hole pairs. As mentioned earlier, a mass of photo-excited carriers generated at the p-ZnO side during UV light (Fig. 6a). The holes in ZnO are directly collected but electrons will pass through the interface through FNT under high reverse bias. The active zone under vis light is composed of the ZnO and Si side,

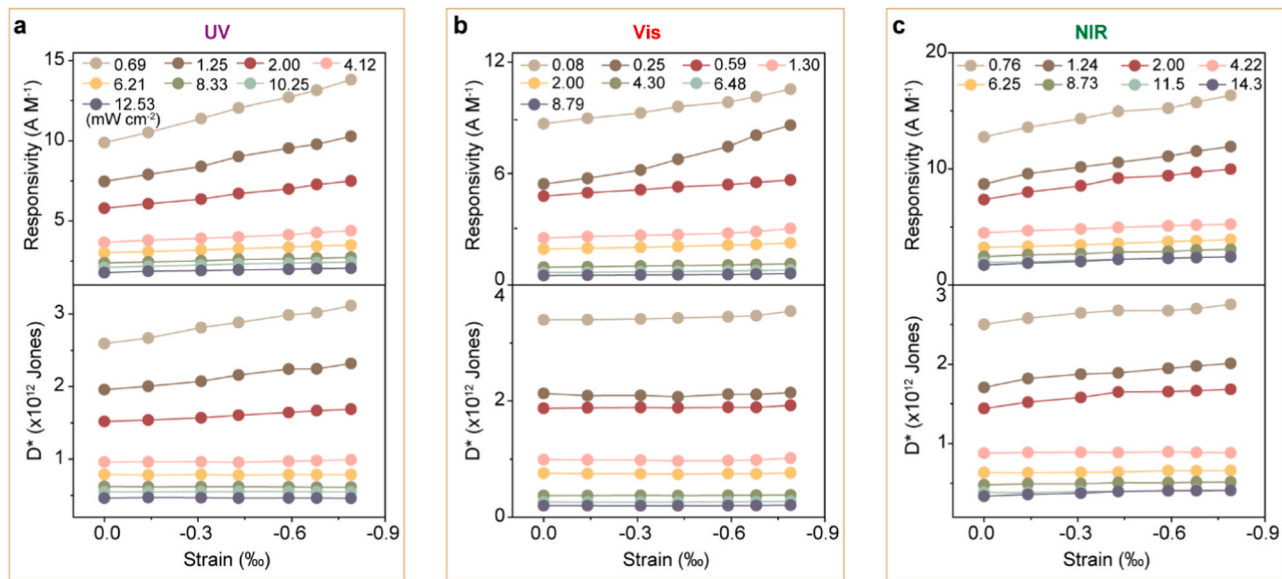


Fig. 5. Piezo-phototronic effect on responsivity and specific detectivity. (a) Responsivity and specific detectivity under 365 nm light excitation and different strains. (b) Responsivity and specific detectivity under 633 nm light excitation and different strains. (c) Responsivity and specific detectivity under 1064 nm light excitation and different strains.

Table 1

Key parameters of photodetectors reported recently.

Material and structure	Responsivity (A W ⁻¹)	Detectivity (Jones)	Response (rise/fall) time (ms)			Ref.
			UV	Vis	NIR	
p-ZnO/Al ₂ O ₃ /n-Si	9.90 (365 nm)	2.60 × 10 ¹² (365 nm)	< 0.18/< 0.23	< 0.13/< 0.07	< 0.14/< 0.18	This work
	8.68 (633 nm)	3.40 × 10 ¹² (633 nm)				
	12.75 (1064 nm)	2.50 × 10 ¹² (1064 nm)				
n-ZnO/Al ₂ O ₃ /p-Si	~1 (442 nm)	-	-	0.26/0.22	-	[50]
	0.65 (1060 nm)	-	-	-	-	
n-ZnO/PbS QD	0.051 (350 nm)	3.4 × 10 ⁸ (350 nm)	< 9000/< 2000	< 500/< 500	< 500/< 500	[4]
	0.0072 (500 nm)	4.9 × 10 ⁷ (500 nm)				
	0.011 (900 nm)	4.2 × 10 ⁷ (900 nm)				
PbS QD-P3HT	~100	< 10 ¹²	< 160/< 110	< 160/< 120	ca. 580/ca. 480	[3]
In ₂ Te ₃ NW	0.3	-	< 10,000/< 10,000	< 100/< 100	< 100/< 100	[2]
Perovskite	0.2-7	-	< 200/< 200	< 100/< 100	-	[9]
ZnO nanorods	0.050	-	< 200	-	-	[33]
2D GaS film	4.7	1.6 × 10 ¹²	< 66/< 66	-	-	[16]
PdSe ₂ TMD	3.35 (532 nm)	1.31 × 10 ⁹	-	< 250	-	[8]
	708 (1064 nm)					
Perovskite/CdS	0.48	2.1 × 10 ¹³	-	0.54/2.2	-	[10]
p-Si/n-ZnO	7.1	7.1 × 10 ⁹	-	> 100/57	-	[35]
Graphene/Ge	0.75	2.53 × 10 ⁹	-	-	< 0.06	[15]

in which case the photo-excited electrons and holes are rapidly separated and collected (Fig. 6b). For NIR light, the active area is dominated by the Si side where electrons are directly collected (Fig. 6c). In general, the photo-excited holes will be confined in the Al₂O₃/Si side due to the large valence band offset, which in turn promotes the recombination of photo-excited holes and electronics. Thanks to the enormous surface area of the ZnO NW array and Si with micro-nano pyramid structure, the incident light can be absorbed effectively so that the number of photo-excited carriers is extremely large. On the other hand, the electrons tunnel through the Al₂O₃ layer will gain greater kinetic energy and collide with the Al₂O₃ lattice under a high electric field, which excites some electrons in the valence band of Al₂O₃, and additional carriers are generated. Even if the Al₂O₃ layer has a large band shift, a high tunneling current could be produced under large reverse bias and certain light intensity. Under compressive strain, positive piezoelectric charge would be induced in ZnO/Al₂O₃ interface due to the non-centrosymmetric structure of ZnO. Most of these piezoelectric charges would be retained without being shielded by local residual free carriers,

thus increasing the electric field density and forming a stronger internal electric field, which leads to more efficient separation and collection of photocarriers. As the strain increases further, the piezoelectric potential bends the depletion layer downward and regulates the effective thickness of the tunneling, thus reducing the accumulated charge density at the ZnO/Al₂O₃ side and leading to an enhance in the photocurrent.

4. Conclusion

In conclusion, we fabricated a high-performance broadband photo-detector with extraordinary sensitivity, a remarkable response time, high responsivity and specific detectivity in the UV to NIR range based on the p-ZnO/Al₂O₃/n-Si heterojunction. It is noteworthy that introducing an Al₂O₃ insulation layer at the p-n junction significantly improves the efficiency of carrier separation and collection, which improves the optoelectronic capability of the device. Besides, the carrier transport properties of devices with different thicknesses of Al₂O₃ are governed by quantum tunneling events (FNT or DT). Specifically, the

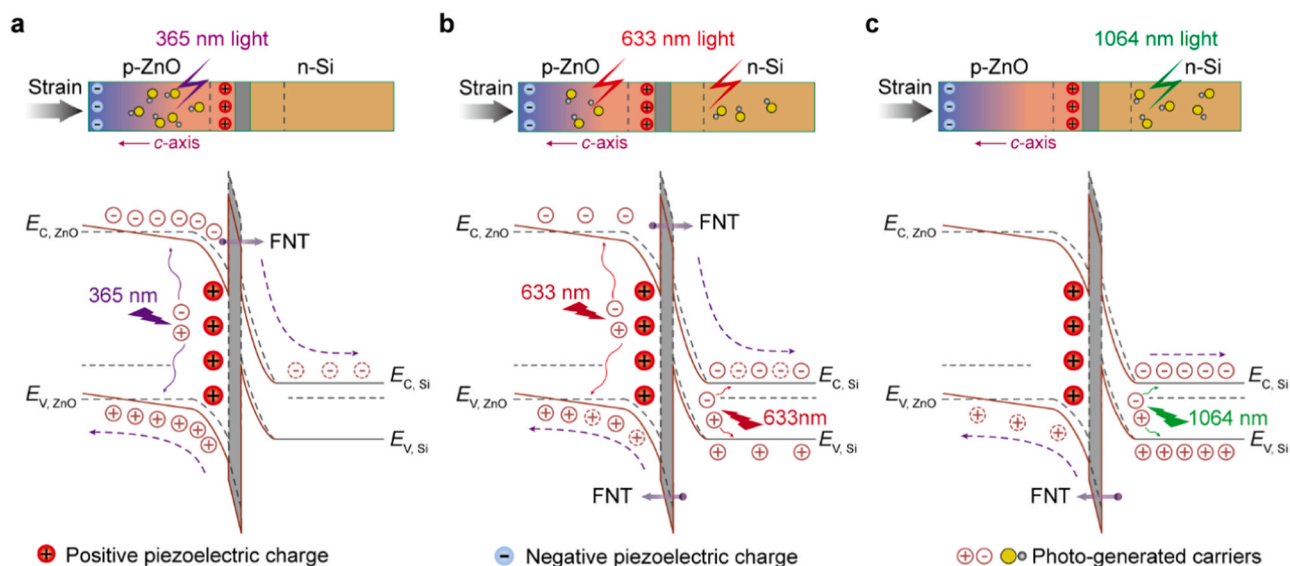


Fig. 6. Working mechanism of the piezo-phototronic effect in p-ZnO/Al₂O₃/n-Si junction. Schematic band diagrams of the heterojunction under various light (a) 365 nm, (b) 633 nm and (c) 1064 nm wavelength and compressive strains to elucidate the carrier regulation mechanism by piezo-phototronic effect.

piezoelectric potential generated in the ZnO side under applied strain regulates the band structure and tunneling barrier distance which affects the transport characteristics of photo-excited carriers under different wavelengths of light excitation. Our experiment conclusions provide a more specific and effective method for realizing an optoelectronic device with wide-spectrum sensing capability without losing excellent photoelectric conversion capability.

CRedit authorship contribution statement

Zhihao Huo: Writing - original draft, Writing - revision and editing, Investigation, Formal analysis, Methodology, Software. **Yufei Zhang:** Writing - reviewing & editing. **Xun Han:** Data curation, Validation. **Wenqiang Wu:** Methodology, Conceptualization. **Wenkai Yang:** Methodology, Investigation. **Xiandi Wang:** Software, Simulation. **Mengmeng Zhou:** Investigation and MS revision and editing. **Caofeng Pan:** Project administration, MS writing and revising, Investigation, Formal analysis, Resources, Supervision, Validation, Funding acquisition.

Declaration of Competing Interest

The authors declare that they have no known competing financial interests or personal relationships that could have appeared to influence the work reported in this paper.

Acknowledgments

The authors thank the support of National Natural Science Foundation of China (No. U20A20166, 61675027, 61805015 and 61804011), National Key R&D Project from Minister of Science and Technology, China (2016YFA0202703), Natural Science Foundation of Beijing Municipality (Z180011), and Shenzhen Science and Technology Program (Grant No. KQTD20170810105439418).

Appendix A. Supporting information

Supplementary data associated with this article can be found in the online version at [doi:10.1016/j.nanoen.2021.106090](https://doi.org/10.1016/j.nanoen.2021.106090).

References

- [1] X. Gong, M. Tong, Y. Xia, W. Cai, J.S. Moon, Y. Cao, G. Yu, C.-L. Shieh, B. Nilsson, A.J. Heeger, High-detectivity polymer photodetectors with spectral response from 300 nm to 1450 nm, *Science* 325 (2009) 1665–1667.
- [2] Z. Wang, M. Safdar, C. Jiang, J. He, High-performance UV–visible-NIR broad spectral photodetectors based on one-dimensional In₂Te₃ nanostructures, *Nano Lett.* 12 (2012) 4715–4721.
- [3] J. Yoo, S. Jeong, S. Kim, J.H. Je, A stretchable nanowire UV-Vis-NIR photodetector with high performance, *Adv. Mater.* 27 (2015) 1712–1717.
- [4] Z. Zheng, L. Gan, J. Zhang, F. Zhuge, T. Zhai, *Adv. Sci.* 4 (2017).
- [5] Y. Jiang, B. Tian, Inorganic semiconductor biointerfaces, *Nat. Rev. Mater.* 3 (2018) 473–490.
- [6] B. Butun, T. Tut, E. Ulker, T. Yelboga, E. Ozbay, *Appl. Phys. Lett.* 92 (2008).
- [7] A.I. Yakimov, V.V. Kirienko, A.A. Bloshkin, V.A. Armbrister, A.V. Dvurechenskii, J. M. Hartmann, Photovoltaic Ge/SiGe quantum dot mid-infrared photodetector enhanced by surface plasmons, *Opt. Express* 25 (2017) 25602–25611.
- [8] Q. Liang, Q. Wang, Q. Zhang, J. Wei, S.X. Lim, R. Zhu, J. Hu, W. Wei, C. Lee, C. Sow, W. Zhang, A.T.S. Wee, High-performance, room temperature, ultra-broadband photodetectors based on air-stable PdSe₂, *Adv. Mater.* 31 (2019), 1807609.
- [9] X. Hu, X. Zhang, L. Liang, J. Bao, S. Li, W. Yang, Y. Xie, High-performance flexible broadband photodetector based on organolead halide perovskite, *Adv. Funct. Mater.* 24 (2014) 7373–7380.
- [10] F. Cao, L. Meng, M. Wang, W. Tian, L. Li, Electrode materials: interfacial lattice-strain-driven generation of oxygen vacancies in an aerobic-annealed TiO₂(B) electrode, *Adv. Mater.* 52/2019, *Adv. Mater.* 31 (2019), 1970367.
- [11] L. Gu, S. Poddar, Y. Lin, Z. Long, D. Zhang, Q. Zhang, L. Shu, X. Qiu, M. Kam, A. Javey, Z. Fan, A biomimetic eye with a hemispherical perovskite nanowire array retina, *Nature* 581 (2020) 278–282.
- [12] X. Wang, H. Shen, Y. Chen, G. Wu, P. Wang, H. Xia, T. Lin, P. Zhou, W. Hu, X. Meng, J. Chu, J. Wang, Solar driven spintronics: sunlight control of interfacial magnetism for solar driven spintronic applications (*Adv. Sci.* 24/2019), *Adv. Sci.* 6 (2019), 1970147.
- [13] X. Liu, F. Zhang, R. Huang, C. Pan, J. Zhu, A new hybrid optical semiconductor based on polymeric iodoplumbate Co-templated by both organic cation and polyiodide anion, *Cryst. Growth Des.* 8 (2008) 4355–4358.
- [14] Y.-L. Wu, K. Fukuda, T. Yokota, T. Someya, *Adv. Mater.* 31 (2019).
- [15] K.E. Chang, C. Kim, T.J. Yoo, M.G. Kwon, S. Heo, S.-Y. Kim, Y. Hyun, J.I. Yoo, H.C. Ko, B.H. Lee, *Adv. Electron. Mater.* 5 (2019).
- [16] Y. Lu, J. Chen, T. Chen, Y. Shu, R.-J. Chang, Y. Sheng, V. Shautsova, N. Mkhize, P. Holdway, H. Bhaskaran, J.H. Warner, *Adv. Mater.* 32 (2020).
- [17] S. Chu, G. Wang, W. Zhou, Y. Lin, L. Chernyak, J. Zhao, J. Kong, L. Li, J. Ren, J. Liu, Electrically pumped waveguide lasing from ZnO nanowires, *Nat. Nanotechnol.* 6 (2011) 506–510.
- [18] C. Pan, L. Dong, G. Zhu, S. Niu, R. Yu, Q. Yang, Y. Liu, Z.L. Wang, High-resolution electroluminescent imaging of pressure distribution using a piezoelectric nanowire LED array, *Nat. Photonics* 7 (2013) 752–758.
- [19] D. You, C. Xu, F. Qin, Z. Zhu, A.G. Manohari, W. Xu, J. Zhao, W. Liu, Interface control for pure ultraviolet electroluminescence from nano-ZnO-based heterojunction devices, *Sci. Bull.* 63 (2018) 38–45.
- [20] L.E. Greene, J.C. Johnson, R. Saykally, P. Yang, Nanowire dye-sensitized solar cells, *Nat. Mater.* 4 (2005) 455–459.

- [21] M. Ahmad, D. Rafi ud, C. Pan, J. Zhu, Investigation of hydrogen storage capabilities of ZnO-based nanostructures, *J. Phys. Chem. C* 114 (2010) 2560–2565.
- [22] W. Guo, C. Xu, G. Zhu, C. Pan, C. Lin, Z.L. Wang, Optical-fiber/TiO₂-nanowire-arrays hybrid structures with tubular counterelectrode for dye-sensitized solar cell, *Nano Energy* 1 (2012) 176–182.
- [23] G. Hu, W. Guo, R. Yu, X. Yang, R. Zhou, C. Pan, Z.L. Wang, Enhanced performances of flexible ZnO/perovskite solar cells by piezo-phototronic effect, *Nano Energy* 23 (2016) 27–33.
- [24] E. Fortunato, P. Barquinha, R. Martins, Oxide semiconductor thin-film transistors: a review of recent advances, *Adv. Mater.* 24 (2012) 2945–2986.
- [25] Z. Huo, Y. Peng, Y. Zhang, G. Gao, B. Wan, W. Wu, Z. Yang, X. Wang, C. Pan, Recent advances in large-scale tactile sensor arrays based on a transistor matrix, *Adv. Mater. Interfaces* 5 (2018), 1801061.
- [26] G. Hu, R. Zhou, R. Yu, L. Dong, C. Pan, Z.L. Wang, Piezotronic effect enhanced Schottky-contact ZnO micro/nanowire humidity sensors, *Nano Res.* 7 (2014) 1083–1091.
- [27] C. Wang, J. Zhao, C. Ma, J. Sun, L. Tian, X. Li, F. Li, X. Han, C. Liu, C. Shen, L. Dong, J. Yang, C. Pan, Detection of non-joint areas tiny strain and anti-interference voice recognition by micro-cracked metal thin film, *Nano Energy* 34 (2017) 578–585.
- [28] X. Wang, M. Que, M. Chen, X. Han, X. Li, C. Pan, Z.L. Wang, *Adv. Mater.* 29 (2017).
- [29] X. Wang, Y. Zhang, X. Zhang, Z. Huo, X. Li, M. Que, Z. Peng, H. Wang, C. Pan, A highly stretchable transparent self-powered triboelectric tactile sensor with metallized nanofibers for wearable electronics, *Adv. Mater.* 30 (2018), 1706738.
- [30] C. Pan, J. Zhai, Z.L. Wang, Piezotronics and piezo-phototronics of third generation semiconductor nanowires, *Chem. Rev.* 119 (2019) 9303–9359.
- [31] X. Han, W. Du, R. Yu, C. Pan, Z.L. Wang, Piezo-phototronic enhanced UV sensing based on a nanowire photodetector array, *Adv. Mater.* 27 (2015) 7963–7969.
- [32] F. Teng, K. Hu, W. Ouyang, X. Fang, *Adv. Mater.* 30 (2018).
- [33] X. Peng, W. Wang, Y. Zeng, X. Pan, Z. Ye, Y. Zeng, Enhanced photoresponse of a high-performance self-powered UV photodetector based on ZnO nanorods and a novel electrolyte by the piezo-phototronic effect, *RSC Adv.* 8 (2018) 33174–33179.
- [34] M. Tang, P. Xu, Z. Wen, X. Chen, C. Pang, X. Xu, C. Meng, X. Liu, H. Tian, N. Raghavan, Q. Yang, Fast response CdS-CdS Te1–CdTe core-shell nanobelt photodetector, *Sci. Bull.* 63 (2018) 1118–1124.
- [35] Z. Wang, R. Yu, X. Wen, Y. Liu, C. Pan, W. Wu, Z.L. Wang, Optimizing performance of silicon-based p-n junction photodetectors by the piezo-phototronic effect, *ACS Nano* 8 (2014) 12866–12873.
- [36] U. Ozgur, Y.I. Alivov, C. Liu, A. Teke, M.A. Reshchikov, S. Dogan, V. Avrutin, S. J. Cho, H. Morkoc, A comprehensive review of ZnO materials and devices, *J. Appl. Phys.* 98 (2005), 041301.
- [37] J.C. Fan, K.M. Sreerkanth, Z. Xie, S.L. Chang, K.V. Rao, Synthesis and cytotoxicity of some novel 21E-benzylidene steroidal derivatives, *Steroids* 78 (2013) 874–879.
- [38] Z. Huo, X. Wang, Y. Zhang, B. Wan, W. Wu, J. Xi, Z. Yang, G. Hu, X. Li, C. Pan, High-performance Sb-doped p-ZnO NW films for self-powered piezoelectric strain sensors, *Nano Energy* 73 (2020), 104744.
- [39] Z.L. Wang, Piezopotential gated nanowire devices: piezotronics and piezo-phototronics, *Nano Today* 5 (2010) 540–552.
- [40] C. Pan, M. Chen, R. Yu, Q. Yang, Y. Hu, Y. Zhang, Z.L. Wang, Progress in piezo-phototronic-effect-enhanced light-emitting diodes and pressure imaging, *Adv. Mater.* 28 (2016) 1535–1552.
- [41] S. Qiao, J. Liu, G. Fu, K. Ren, Z. Li, S. Wang, C. Pan, ZnO nanowire based CIGS solar cell and its efficiency enhancement by the piezo-phototronic effect, *Nano Energy* 49 (2018) 508–514.
- [42] X. Wang, D. Peng, B. Huang, C. Pan, Z.L. Wang, Piezophotonic effect based on mechanoluminescent materials for advanced flexible optoelectronic applications, *Nano Energy* 55 (2019) 389–400.
- [43] C. Pan, Z. Luo, C. Xu, J. Luo, R. Liang, G. Zhu, W. Wu, W. Guo, X. Yan, J. Xu, Z. L. Wang, J. Zhu, Wafer-scale high-throughput ordered arrays of Si and coaxial Si/Si(1-x)Ge(x) wires: fabrication, characterization, and photovoltaic application, *ACS Nano* 5 (2011) 6629–6636.
- [44] X. Li, M. Chen, R. Yu, T. Zhang, D. Song, R. Liang, Q. Zhang, S. Cheng, L. Dong, A. Pan, Z.L. Wang, J. Zhu, C. Pan, Enhancing light emission of ZnO-nanofilm/Si-micropillar heterostructure arrays by piezo-phototronic effect, *Adv. Mater.* 27 (2015) 4447–4453.
- [45] W. Chen, R. Liang, J. Wang, S. Zhang, J. Xu, Enhanced photoresponsivity and hole mobility of MoTe₂ phototransistors by using an Al₂O₃ high-κ gate dielectric, *Sci. Bull.* 63 (2018) 997–1005.
- [46] R. Yang, Y. Qin, L. Dai, Z.L. Wang, Power generation with laterally packaged piezoelectric fine wires, *Nat. Nanotechnol.* 4 (2009) 34–39.
- [47] L. Dong, S. Niu, C. Pan, R. Yu, Y. Zhang, Z.L. Wang, Piezo-phototronic effect of CdSe nanowires, *Adv. Mater.* 24 (2012) 5470–5475.
- [48] F. Zhang, Y. Ding, Y. Zhang, X. Zhang, Z.L. Wang, Piezo-phototronic effect enhanced visible and ultraviolet photodetection using a ZnO-CdS core-shell micro/nanowire, *ACS Nano* 6 (2012) 9229–9236.
- [49] W. Dai, X. Pan, S. Chen, C. Chen, W. Chen, H. Zhang, Z. Ye, ZnO homojunction UV photodetector based on solution-grown Sb-doped p-type ZnO nanorods and pure n-type ZnO nanorods, *RSC Adv.* 5 (2015) 6311–6314.
- [50] H. Zou, X. Li, G. Dai, W. Peng, Y. Ding, Y. Zhang, A.C. Wang, S.L. Zhang, C. Xu, S.-L. Zhang, Z.L. Wang, Dramatically enhanced broadband photodetection by dual inversion layers and Fowler-Nordheim tunneling, *ACS Nano* 13 (2019) 2289–2297.
- [51] G. Nazir, H. Kim, J. Kim, K.S. Kim, D.H. Shin, M.F. Khan, D.S. Lee, J.Y. Hwang, C. Hwang, J. Suh, J. Eom, S. Jung, *Nat. Commun.* 9 (2018).

- [52] H.-M. Li, D. Lee, D. Qu, X. Liu, J. Ryu, A. Seabaugh, W.J. Yoo, *Nat. Commun.* 6 (2015).
- [53] H.-L. Lu, M. Yang, Z.-Y. Xie, Y. Geng, Y. Zhang, P.-F. Wang, Q.-Q. Sun, S.-J. Ding, D. W. Zhang, In situ metalorganic chemical vapor deposition of Al₂O₃ on N-face GaN and evidence of polarity induced fixed charge, *Appl. Phys. Lett.* 104 (2014), 263511.
- [54] T. Ikuno, H. Okamoto, Y. Sugiyama, H. Nakano, F. Yamada, I. Kamiya, *Appl. Phys. Lett.* 99 (2011).



Zhihao Huo received his undergraduate degree from the University of Jinan in 2016. Currently he is pursuing his Ph.D. degree under the supervision of Prof. Caofeng Pan at Beijing Institute of Nanoenergy and Nanosystems, Chinese Academy of Sciences. His current research interests focus on low-dimensional piezoelectric semiconductor micro/nanophotonic electric function device.



Yufei Zhang received his master's degree in Materials Science & Engineering from Beihang University in 2019. He is currently a Ph.D. Candidate majored in Nanomaterials and devices at Beijing Institute of Nanoenergy and Nanosystems, CAS. His research focuses on stretchable transparent materials and wireless wearable electronic devices.



Dr. Xun Han received his B.S. degree (2012) from Shandong University and his Ph.D. degree (2017) from the Beijing Institute of Nanoenergy and Nanosystems, Chinese Academy of Sciences, China. He carried out postdoctoral research work at Northeastern University (U.S.). He joined Shenzhen University as a Research Associate Professor in 2019. His research interests mainly focus on the fields of piezophototronics effect for advanced optoelectronic devices.



Wenqiang Wu is currently a Ph.D. candidate in the College of Materials Science and Engineering, Hunan University. Since 2016, he has been a visiting student in the group of Prof. Caofeng Pan at Beijing Institute of Nanoenergy and Nanosystems, Chinese Academy of Sciences. His research focuses on the controllable synthesis of perovskite materials and the fabrication of high-performance photodetector array.



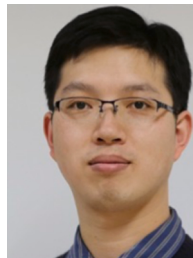
Wenkai Yang received his undergraduate degree from the Central South University in 2018. Currently he is pursuing his master's degree under the supervision of Prof. Caofeng Pan at Beijing Institute of Nanoenergy and Nanosystems, Chinese Academy of Sciences. His current research interests focus on two-dimensional material van der Waals heterojunction.



Dr. Mengmeng Zhou obtained her M.S. degree in Management from University of Southampton, UK in 2015 and B.S. degree in Mechanical Engineering from University of Sussex, UK in 2014. She joined National Nanoscience Center as assistant engineer since 2016–2017. Then started her Ph.D. in 2017 in Chemical Engineering, Monash University and received the Ph.D. degree 2020. She had been a research fellow in Chemical Engineering, Monash University since September, 2020. Her research interests is focusing on modeling and analysis of solid-liquid system using CFD-DEM method, and swell particles in liquid system.



Dr. Xiandi Wang received his Ph.D. degree in condensed matter physics from the University of Chinese Academy of Sciences in 2016. He had been a postdoc fellow in the group of Professor Zhong Lin Wang at National Center for Nanoscience and Technology. He had been an associate professor in the group of Prof. Caofeng Pan at Beijing Institute of Nanoenergy and Nanosystems, CAS since 2018. Now he works at Zhejiang University. His research interests mainly focus on the fields of piezo-photonic effect and triboelectric nanogenerator for fabricating novel flexible large-scale tactile sensor matrix and stretchable electronics.



Dr. Caofeng Pan received his B.S. degree (2005) and his Ph.D. (2010) in Materials Science and Engineering from Tsinghua University, China. He then joined the Georgia Institute of Technology as a postdoctoral fellow. He is currently a professor and a group leader at Beijing Institute of Nanoenergy and Nanosystems, Chinese Academy of Sciences since 2013. His main research interests focus on the fields of piezotronics/piezo-phototronics for fabricating new electronic and optoelectronic devices, nano-power source (such as nanofuel cell, nano biofuel cell and nanogenerator), hybrid nanogenerators, and self-powered nanosystems. Details can be found at <http://www.piezotronics.cn>.